Int J Adv Manuf Technol (2016) 87:1095–1104
DOI 10.1007/s00170-016-8599-z

ORIGINAL ARTICLE

Improving the structure-property of aluminum alloy friction stir weld by using a non-shoulder-plunge welding tool

H. J. Zhang[1] · M. Wang[1] · Z. Zhu[1] · X. Zhang[1] · T. Yu[1] · G. X. Yang[1]

Received: 4 September 2015 / Accepted: 2 March 2016 / Published online: 9 March 2016

Abstract In order to improve the joint performances by controlling the thermal effect of tool shoulder, a non-shoulder-plunge (NSP) welding tool is utilized to conduct friction stir welding (FSW) of an Al-Mg aluminum alloy in this paper. Sound FSW joint is successfully produced by using the NSP welding tool. In contrast to conventional FSW (C-FSW), the thermal effect of tool shoulder is effectively reduced by NSP-FSW, leading to a significant size reduction of shoulder-affected zone in the joint. Besides, the NSP-FSW joint shows finer grain structures in the stir zone and thermo-mechanically affected zone, and exhibits lower extents of grain coarsening, dislocation polygonization, and particle dissolution in the heat-affected zone. Hardness maps show that the softening region width of NSP-FSW joint is only nearly half that of C-FSW joint and the NSP-FSW joint exhibits higher hardness in the heat-affected zone than C-FSW joint. The tensile test results indicate that the joint efficiency is improved from 89 % of C-FSW joint to 97 % by the NSP-FSW process.

Keywords Friction stir welding · Aluminum alloy · Non-shoulder-plunge welding tool · Structure-property

✉ H. J. Zhang
zhanghuijie@sia.cn

[1] State Key Laboratory of Robotics, Shenyang Institute of Automation Chinese Academy of Sciences, Shenyang 110000, People's Republic of China

1 Introduction

Friction stir welding (FSW) has been successfully utilized to weld various types of aluminum alloys since its invention [1]. As far as the non-heat treatable aluminum alloys are concerned, sound joints with properties equivalent to the base metal can be fabricated by FSW process. While in regard to the heat treatable aluminum alloys or work hardened aluminum alloys, the thermal effect of welding tool generally causes local softening to occur in the joints during FSW and the mechanical properties of joints are lowered in contrast to the base metal [2].

Controlling the heat input into workpiece is an effective approach to improve the microstructure evolution and mechanical properties of FSW joints. The heat input during FSW is generated by the interaction between welding tool and workpiece. The FSW tool is mainly composed of two parts, i.e., tool shoulder and tool pin. The tool shoulder contributes primarily to the heat generation during the welding [3–5]. Therefore, it is rather important to control the heat input from tool shoulder in order to reduce the negative effects of welding thermal cycles. In order to do this, the liquid-cooled FSW process has been extensively investigated in previous studies. Fratini et al. [6] considered in-process heat treatment with water flowing on the top surface of the samples during FSW. The results showed that the peak temperature around tool shoulder is notably lowered and the tensile strength of the joint was improved by the cooling action. With the aim to take full advantage of external liquid cooling action, underwater friction stir welding of aluminum alloys was investigated by several researchers [7–10]. Compared with conventional FSW, it was found that the size of shoulder-affected zone was reduced and the strength improvement was acquired under the water cooling action. The positive effects of external liquid cooling on structure-property improvements of FSW

joints have been demonstrated by these investigations; however, the employment of external liquid cooling inevitably increases the complexity of both the system and process during FSW, which would restrict the use of FSW for practical production.

In regard to FSW process, tool rotation speed, welding speed, and shoulder plunge depth are three important parameters determining the heat input levels [11]. To achieve the superior joint performances, the rotation speed and welding speed were mostly optimized to reduce the heat input as much as possible on the premise of avoiding the defect formation during FSW [11–13]. However, the shoulder plunge depth was rarely optimized during the control of heat input levels in previous studies. This should be attributed to that the value of shoulder plunge depth is largely determined by weld surface formation quality. If the shoulder plunge depth is too low or too high, weld surface defects such as groove and flash are more prone to be formed in the joints. Thereby, in contrast to the rotation speed and welding speed, the shoulder plunge depth generally varies in a relatively narrow range for sound weld appearance formation [14–16].

The use of shoulder plunge depth is a fundamental characteristic of conventional FSW. Actually, the value of shoulder plunge depth reflects the extent of interaction between tool shoulder and workpiece. From the perspective of optimization of shoulder plunge depth, if the defect-free FSW joints can be produced at a zero shoulder plunge depth, the interaction level between tool shoulder and workpiece as well as the thermal effect of tool shoulder is believed to be weakened on the basis of conventional FSW, and further improvement of joint performances is expected to be obtained. Based on this assumption, a novel non-shoulder-plunge (NSP) FSW process is explored in this study, during which a zero shoulder plunge depth is applied to welding tool. This work is aimed to fundamentally control the heat input from tool shoulder during FSW by weakening the interaction between tool shoulder and workpiece, and resultantly, to improve the structure-property of FSW joints.

2 Experimental procedure

The base metal (BM) used for this investigation was an 8-mm-thick 5052 aluminum alloy plate in H32 condition, which is a type of antirust aluminum alloy belonging to Al-Mg series. The chemical compositions and mechanical properties of the BM are listed in Table 1. Figure 1 shows the microstructures of BM, and the following observations are made. First, the BM exhibits coarse elongated grains (40.3 ± 8.7 μm in size) parallel to the rolling direction due to the work hardening (see Fig. 1a). Second, a great amount of grains from BM are found to contain high-density dislocations with a network structure (see Fig. 1b). Third, many block-shaped second-phase particles are distributed in the Al matrix (see Fig. 1c). The energy dispersive spectrometer (EDS) analysis reveals that the second-phase particles have a Mg to Si ratio (at. pct) of close to 2:1, corresponding to the stoichiometry of the Mg_2Si phase.

The dimension of welding samples was 300 mm long by 100 mm wide. Butt welds were made along the longitudinal direction (perpendicular to the rolling direction) of the welding samples using an FSW machine. The welds were made in displacement control rather than z-axis load control. K-type thermocouples were used to measure the temperature of the samples during FSW. The thermocouples were located at the top surfaces of samples on the advancing side (AS) with distances of 15 and 20 mm from weld center.

After welding, the joints were all cross-sectioned perpendicular to the welding direction for metallographic analyses and mechanical tests. The cross sections of the metallographic specimens were polished using a diamond paste, etched with Keller's reagent, and observed by an optical microscopy (Olympus DSX500). Microstructural analyses were carried out on the weld midplane, and the exact locations where the microstructures were extracted included the center of stir zone (SZ), the thermo-mechanically affected zone (TMAZ) adjacent to SZ on the AS, and the heat-affected zone (HAZ) adjacent to TMAZ on the AS and the BM. The grain structures were analyzed by electron back-scattered diffraction (EBSD). The EBSD data was collected using a JEOL JSM-7001F scanning electron microscope and processed with TSL OIM Analysis 6 software. Transmission electron microscopy (TEM PHILIPS CM12) was used to determine the substructures. The foil disk specimens for TEM were cut parallel to the welding direction and prepared through double jet electro-polishing using a solution of 30 % nitric acid in methanol (18 V and −35 °C). A FEI Quanta 250 FEG scanning electron microscope was utilized to evaluate the distribution of second-phase particles.

Microhardness was measured across the polished cross sections at a horizontal spacing of 1 mm and a vertical spacing of 1.3 mm. The testing load was 1.96 N for 10 s. The transverse tensile specimens were prepared with reference to China National Standard (GB/T2651-2008) (equivalent to American Standard ASTM B557-2). Tensile properties of each joint were evaluated using three tensile specimens cut from the same joint. It is noted that all the specimens were extracted from the middle part of the joints where the steady state of the FSW process was achieved. The room temperature tensile test was carried out at a crosshead speed of 1 mm/min using an electron universal testing machine (Instron 5566).

Table 1 Chemical compositions and mechanical properties of 5052-H32 aluminum alloy

Chemical compositions (wt%)								Mechanical properties	
Al	Mg	Si	Fe	Cr	Cu	Mn	Zn	Tensile strength	Elongation
Bal.	2.2~2.8	0.25	0.4	0.15~0.35	0.1	0.1	0.1	225 MPa	24 %

3 Results and discussion

3.1 Determination of NSP welding tool features

Limited by the configuration of welding tool, it is rather difficult to produce sound joint by using a zero shoulder plunge depth in conventional FSW. In order to successfully conduct NSP-FSW, the proper design of welding tool, especially the tool shoulder, is of great importance. The tool shoulder has three functions during the formation of friction stir weld: (1) constraining the heated material beneath the shoulder end surface, (2) directing the inward flow of plastic material, and (3) producing the downward forging action for weld consolidation and frictionally heating the surface regions of the workpiece [17]. To constrain the heated material beneath tool shoulder, a concave feature is machined on the shoulder end surface in this study (see Fig. 2a). During NSP-FSW, the concave shoulder end surface, the weld top surface, and the side surface of tool pin together compose a closed space. The flowing plastic material is then contained and trapped in the space during welding. Scrolls are among the most useful geometrical features used for developing an inwardly directed traction force under tool shoulder during FSW [17–19]; therefore, three equally spaced scrolls were machined on the concave shoulder (see Fig. 2b), which prevents the plastic material under shoulder from slipping out during NSP-FSW. In order to improve the material flow and nugget integrity, the concave angle and diameter of tool shoulder are properly designed to afford sufficient forging force and frictional heat to the workpiece. The determined NSP welding tool had a 26-mm-diameter shoulder and a 7.8-mm-length conical right-hand screwed pin.

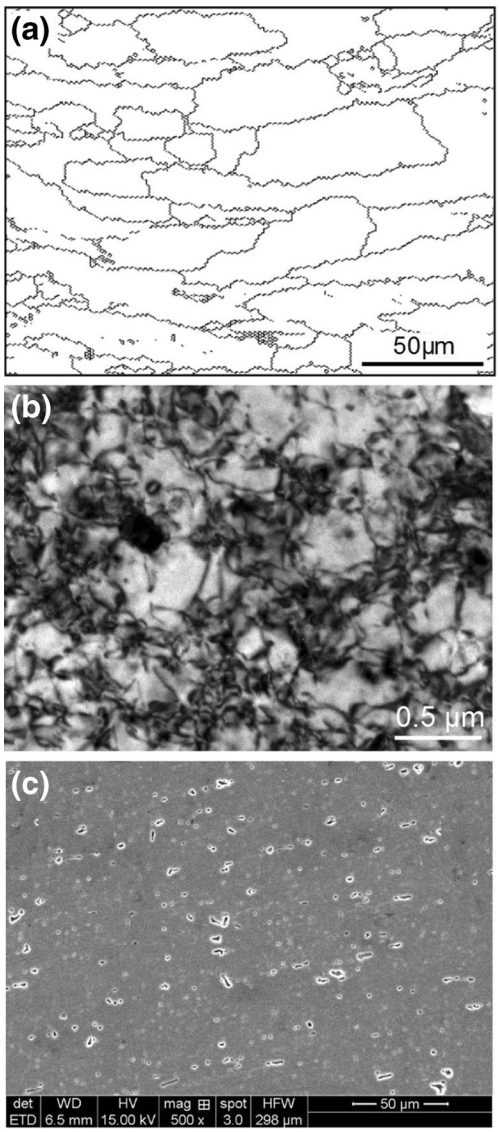

Fig. 1 Microstructures of the base metal: **a** grain structures, **b** dislocation structures, and **c** second-phase particles

In order to deeply illustrate the characteristic of NSP-FSW process, the conventional FSW (C-FSW), during which a shoulder plunge depth was utilized, was also conducted on the same BM in this paper. The welding tool used for C-FSW had a smooth concave shoulder with the diameter of 22 mm and the same tool pin as used in NSP-FSW (see Fig. 2c, d). Note that the geometrical size of the welding tool used in C-FSW was the optimal result of our previous investigations.

A rotation speed of 600 rpm and a welding speed of 100 mm/min were used for both NSP-FSW and C-FSW. The shoulder plunge depth was 0 mm, and the tool tilting angle was 0° during NSP-FSW. In our previous investigations on C-FSW of the BM used in this study, when shoulder plunge depth varied from 0.05 to 0.3 mm at an interval of 0.05 mm, it was found that 0.2 mm was the minimum shoulder plunge depth for producing defect-free joints at the chosen welding parameters above mentioned; therefore, a shoulder plunge depth of 0.2 mm was applied to welding tool in C-FSW. The tool titling angle was set to 2.5° during C-FSW.

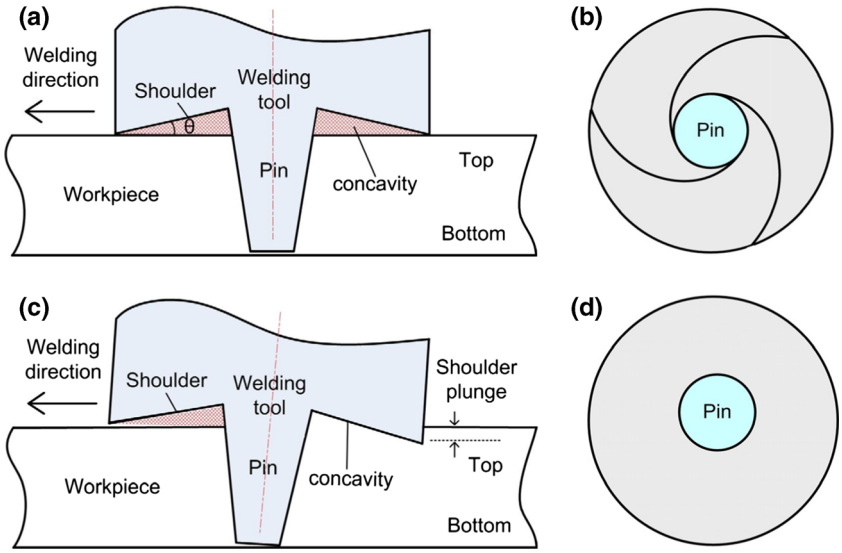

Fig. 2 Schematic views of FSW process and tool features: **a** NSP-FSW, **b** shoulder end surface of NSP-FSW tool, **c** C-FSW, and **d** shoulder end surface of C-FSW tool

3.2 Weld formation quality

Figure 3 presents the cross sections of the FSW joints. It should be noted that the retreating side is on the left, while the advancing side is on the right for each cross section in the figure and throughout the whole paper. The base material is severely deformed under the tool stirring action, and two deformed zones, i.e., the SZ and TMAZ, can be clearly observed in the both joints (see Fig. 3a, b). The borders of the SZ and TMAZ, depicted by the dashed lines in Fig. 3, are determined by the grain structure features. During C-FSW, a severe shoulder stirring effect is exerted to the base material due to the application of shoulder plunge depth; hence, an evident shoulder-affected zone is observed in the SZ, as marked in Fig. 3c. By contrast, there is nearly a complete absence of shoulder-affected zone at the top of NSP-FSW joint (see Fig. 3d). During NSP-FSW, the material beneath tool shoulder is mainly from the pin-sheared material. The pin-sheared material is extruded upward into the concave of shoulder and then flows with the rotating shoulder under the inwardly directed traction force of scrolls; finally, it fills the hole at the rear of welding tool, resulting in the weld formation. Since the shoulder itself applies rather weak stirring effect to the base material due to the application of a zero shoulder plunge depth, the shoulder-affected zone almost disappears completely in the NSP-FSW joint. Further comparison finds that the TMAZ is also narrowed in the NSP-FSW joint, further confirming the limitation of material plastic deformation around the welding tool during NSP-FSW.

3.3 Welding thermal cycles

Figure 4 shows the temperature histories of FSW joints. At each measured location, the NSP-FSW joint shows lower peak temperature than the C-FSW joint; furthermore, the NSP-FSW joint exhibits shorter dwelling time above a given

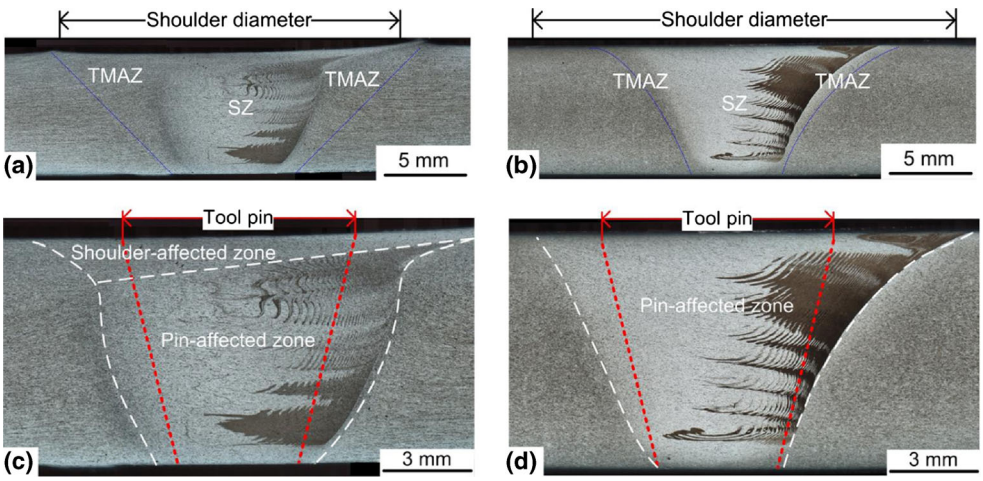

Fig. 3 Cross sections of the FSW joints: **a** C-FSW joint, **b** NSP-FSW joint, **c** enlarged view of C-FSW joint, and **d** enlarged view of NSP-FSW joint

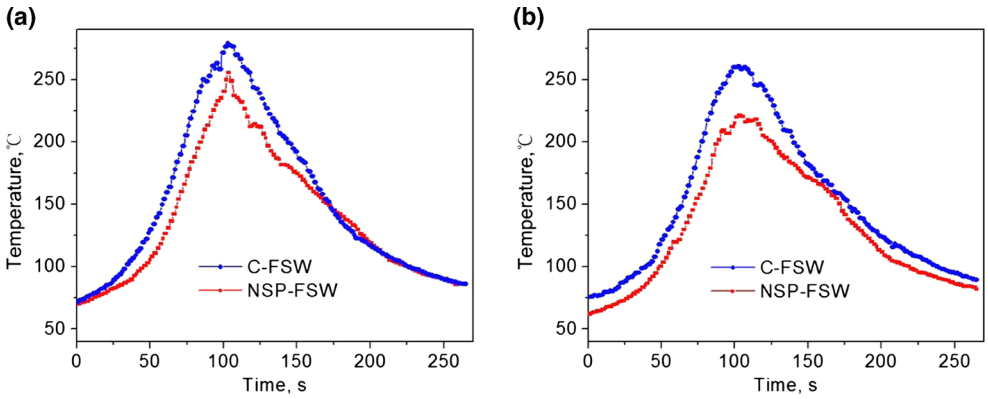

Fig. 4 Welding thermal cycles during FSW: **a** 15 mm from weld center and **b** 20 mm from weld center

temperature in the welding thermal cycles. Since the tool pins used for C-FSW and NSP-FSW are the same, the different thermal cycles between the both joints should be mainly resulted from the variation of shoulder thermal effect during the welding. Obviously, the thermal effect of tool shoulder has been effectively weakened owing to the application of a zero shoulder plunge depth. Because of this, the plastic deformation level around welding tool is lowered, leading to the size reduction of shoulder-affected zone and the narrowing of TMAZ in NSP-FSW joint.

The intrinsic reason for the different thermal evolutions between C-FSW joint and NSP-FSW joint can be explained as follows. Although the tool shoulders used in C-FSW and NSP-FSW both have the concave feature, their positions relative to workpiece top surface are of essential difference. For C-FSW, the tool shoulder is embedded into the workpiece to a certain distance due to the application of shoulder plunge depth, which directly exerts severe stirring effect to the base material. In contrast, the concave shoulder of NSP-FSW tool is not embedded into the workpiece during welding. The rel-

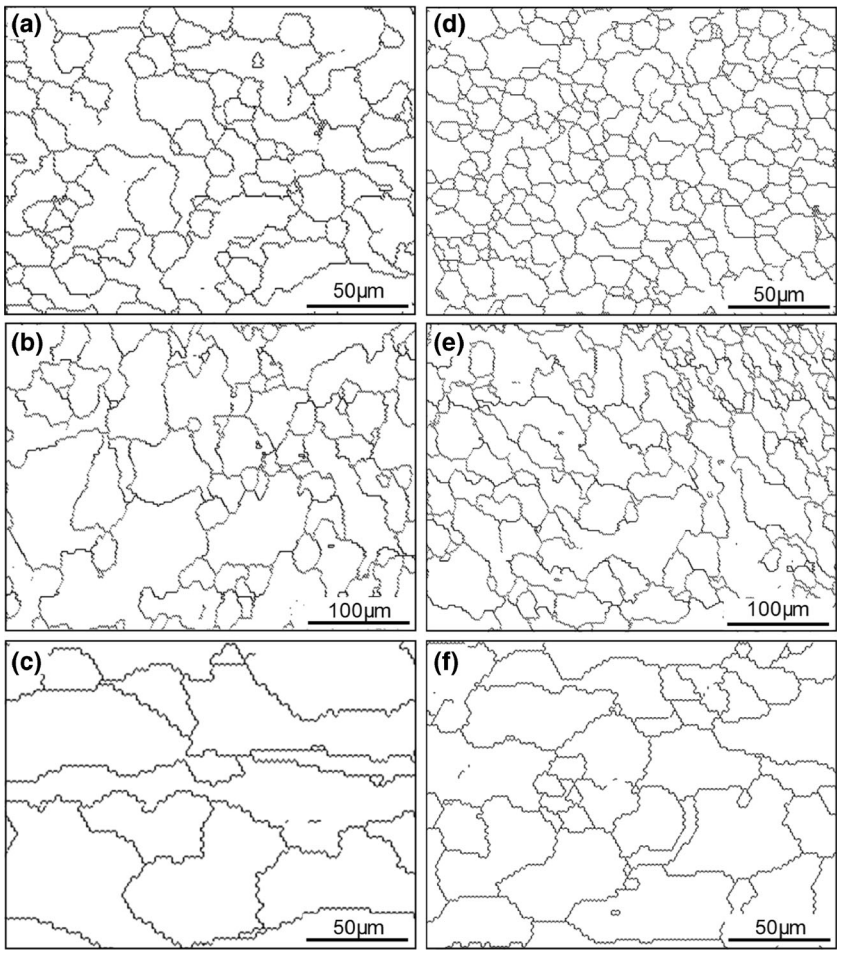

Fig. 5 Grain structures of different zones of the joints: **a**–**c** SZ, TMAZ, and HAZ of C-FSW joint, and **d**–**f** SZ, TMAZ, and HAZ of NSP-FSW joint

ative distance from the shoulder edge to the top surface of workpiece is not negative but equals to zero. This not only limits the heat generation due to weakening of shoulder/workpiece interaction but also makes the frictional heat generated by tool shoulder to transfer a longer distance to the weld. These two factors together lead to the weakening of shoulder thermal effect during NSP-FSW.

3.4 Microstructural evolutions

Figure 5 shows the grain structures extracted from different zones of the both joints. In comparison with BM, the joints have experienced significant grain refinement in the SZ and TMAZ due to dynamic recovery and recrystallization, as seen from Fig. 5a, b, d, e. The grain sizes of the SZ and TMAZ of NSP-FSW joint are 9.8 ± 4.8 and 35.5 ± 9.4 μm, respectively, smaller than the corresponding values (14.2 ± 6.5 and 43.1 ± 15.2 μm) of C-FSW joint. The weld experiences lower temperatures and shorter thermal cycles during NSP-FSW, static grain growth after intense plastic deformation is less significant, and thus, finer grains are formed in these two zones. In the HAZ (see Fig. 5c, f), the grain sizes of C-FSW joint and NSP-FSW joint are 58.3 ± 14.7 and 46.2 ± 10.3 μm, respectively, both larger than the grain size of BM. That is to say, grain coarsening has occurred in the HAZs during FSW. Comparatively, the smaller grain size of NSP-FSW joint implies that the grain coarsening level has been effectively controlled during NSP-FSW.

The dislocation structures of joints are presented in Fig. 6, which also exhibit different features between C-FSW joint and NSP-FSW joint. In the HAZ, both the joints possess lower dislocation densities than the BM (see Figs. 6a, d and 1b), which should be attributed to the migration and polygonization of dislocations during the annealing process. Apparently, large extent of annealing has occurred in the HAZ of C-FSW joint, leading to the significant recovered structures in this zone (see Fig. 6a). The weak welding thermal cycles during NSP-FSW retard the dislocation polygonization, and a certain amount of dislocations with network structure are still observed in the HAZ (see Fig. 6d). With respect to the TMAZ and SZ, the dislocation density is dramatically decreased in the both joints (see Fig. 6b, c, e, f). Further observation reveals that the C-FSW joint contains more recovered structures and dislocations within the grains. As the dynamic recovery and recrystallization progress during FSW, dislocation is continuously generated by the intense plastic deformation [20, 21];

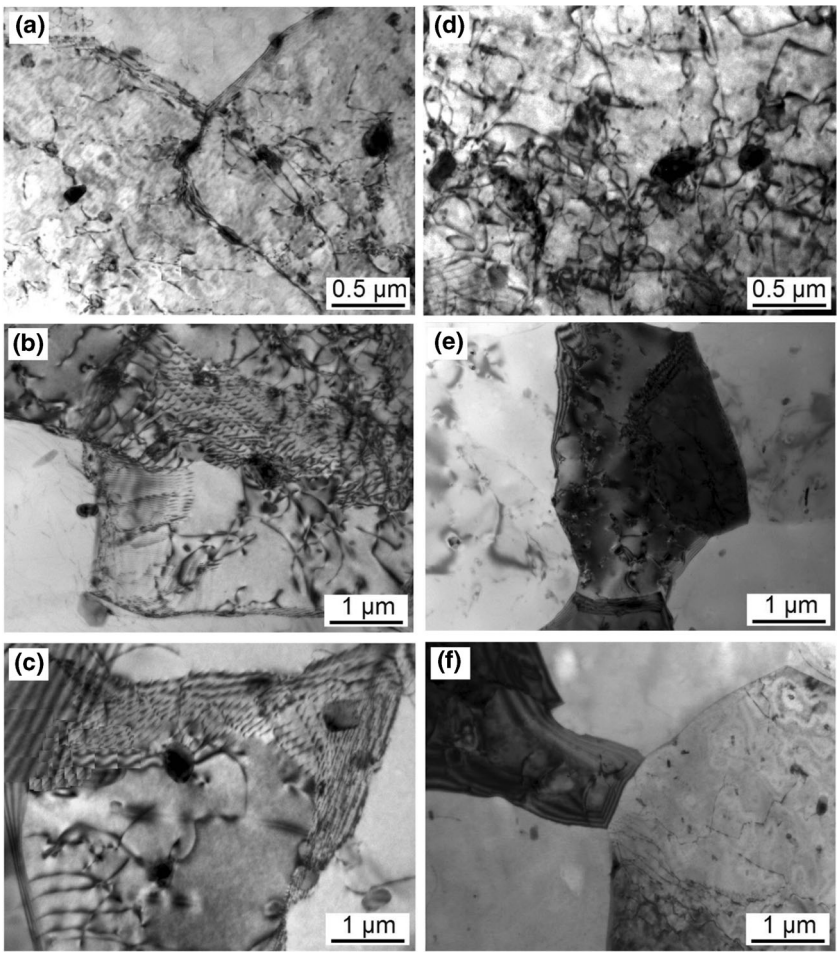

Fig. 6 Dislocation structures of different zones of the joints: **a**–**c** HAZ, TMAZ, and SZ of C-FSW joint, and **d**–**f** HAZ, TMAZ, and SZ of NSP-FSW joint

simultaneously, the slip and pile-up of the generated dislocations promote the formation of recovered structures. The welding tool exerts stronger thermal effect to the C-FSW joint, the induced larger stain rate during FSW then results in the higher densities of dislocations and recovered structures.

Figure 7 shows the distribution of second-phase particles in various zones of the C-FSW joint and NSP-FSW joint. The following observations deserve attention. First, for each joint, the distribution density of second-phase particles is decreased progressively from HAZ to SZ, illustrating that the dissolution of second-phase particles has occurred during FSW and the dissolution level is gradually improved as the weld center is approached. Second, for each zone, especially the HAZ, the size and distribution density of second-phase particles in NSP-FSW joint are higher than those in C-FSW joint. The particles in the HAZ of NSP-FSW joint have an average size of 2.75 ± 0.67 μm and an area fraction of 0.033 (see Fig. 7d), similar to those of BM (2.66 ± 0.36 μm and 0.045, respectively). This means that the particle evolution is slightly affected by the welding thermal cycles during NSP-FSW. However, the average size and area fraction of second-phase particles are only 1.92 ± 0.45 μm and 0.009 in the HAZ of C-FSW joint (Fig. 7a), suggesting a larger extent of particle dissolution under the elevated temperature.

The above analyses indicate that the grains, dislocation structures, and second-phase particles have experienced complex evolutions during FSW. Solid solution strengthening, second-phase particle strengthening, grain boundary strengthening, and dislocation strengthening are the known mechanisms that contribute to the mechanical properties of friction stir-welded work-hardened aluminum alloys [22–24]. Therefore, these microstructural evolutions must have influences on the mechanical properties of FSW joints. The structure-property correlations need further exploration.

3.5 Hardness distributions

In order to further illuminate the characteristics of NSP-FSW process, the microhardness map was made across the two-dimensional cross sections of the joints, as shown in Fig. 8.

The hardness of BM varies in the range of 62–70 Hv. From BM to HAZ, the grain coarsening, the drop of dislocation density, and the dissolution of second-phase particles take place during FSW cause the hardness to decrease gradually

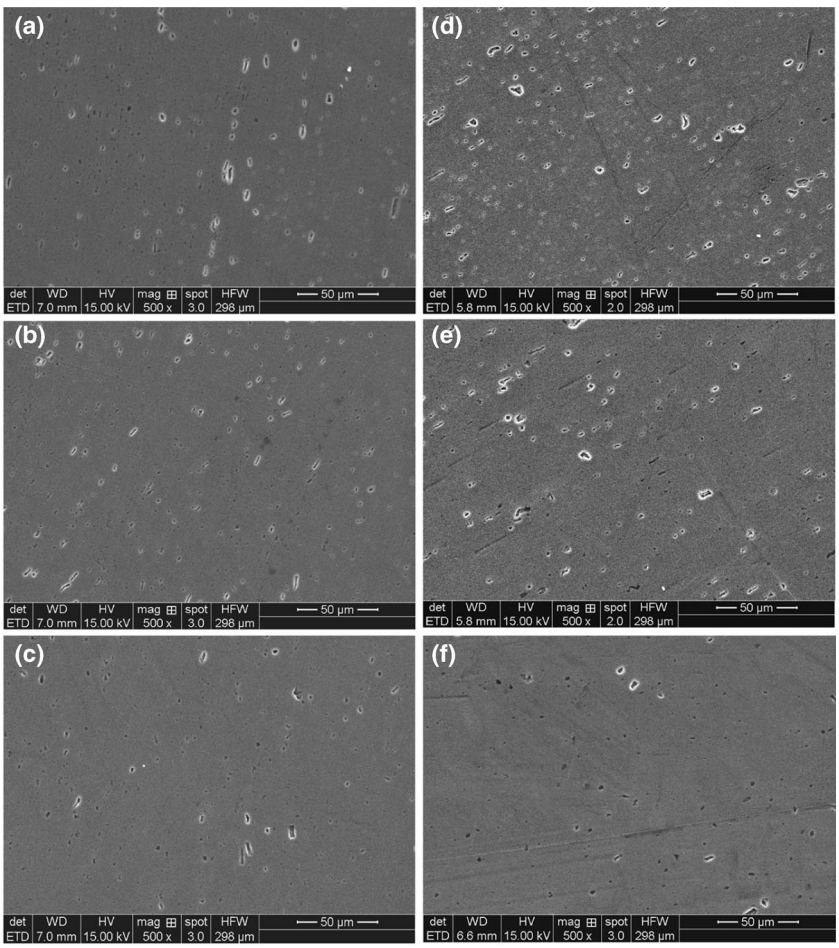

Fig. 7 Second-phase particles distributed in different zones of the joints: **a**–**c** HAZ, TMAZ, and SZ of C-FSW joint, and **d**–**f** HAZ, TMAZ, and SZ of NSP-FSW joint

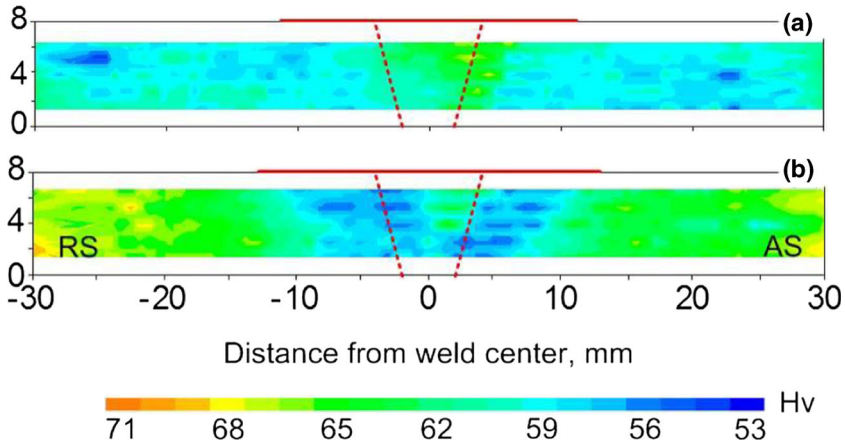

Fig. 8 Hardness distribution maps of FSW joints: **a** C-FSW joint and **b** NSP-FSW joint

in the both joints. As the SZ is approached, the strengthening effects from dislocation and second-phase particles are further lowered. Nevertheless, the grain refinement exerts positive effect on the strength improvement according to Hall-Petch relationship; additionally, the particle dissolution increases the concentration of solute atoms, which can also improve the strength through dislocation-solute atom interaction. Because of this, the hardness is not decreased but shows an increase trend, leading to the occurrence of "W" type hardness profiles in the two joints. Threadgill et al. [24] concluded that for the FSW joints of work-hardened aluminum alloys, the hardness minimum was typically in the nugget where the fully recrystallized structure was formed, and the hardness profiles commonly presented a "U" type. However, the W type hardness profiles are acquired in this research, demonstrating the positive effects of grain refinement and particle dissolution on the hardness recovery in deformed zones.

The C-FSW joint has a rather wide softening region (~55 mm), while the NSP-FSW joint only has a softening region width of ~25 mm, nearly half that of C-FSW joint (see Figs. 8 and 9). This means that the affecting area of welding thermal cycles has been significantly reduced by NSP-FSW. The lowest hardness region of C-FSW joint is lying in the HAZ, far from the weld center, while that of NSP-FSW joint is just located at the HAZ adjacent to pin periphery. Owing to the controlling of heat input levels, the grain coarsening, dislocation polygonization, and particle dissolution are all retarded in the HAZ during NSP-FSW and thus the NSP-FSW joint possesses higher hardness minimum than the C-FSW joint.

3.6 Tensile properties

Figure 10 displays the tensile properties of the both joints. The C-FSW joint presents a tensile strength of 200 MPa, equivalent to 89 % of that of BM. By contrast, the tensile strength of NSP-FSW joint is 218 MPa, reaching 97 % of that of BM. The small error bars of the tensile strength values demonstrate the consistency and accuracy of the tensile test result. It is thus concluded that the NSP-FSW process can effectively improve the tensile properties of the C-FSW joint. The elongations of C-FSW joint and NSP-FSW joint are 24 and 24.3 %, respectively, comparable with the elongation of BM.

Figure 11 shows the fracture features of the joints. The C-FSW joint fails in the HAZ, the fracture location is outside the weld track and lying in the lowest hardness region (see Fig. 11a). The fracture of NSP-FSW joint during tensile test

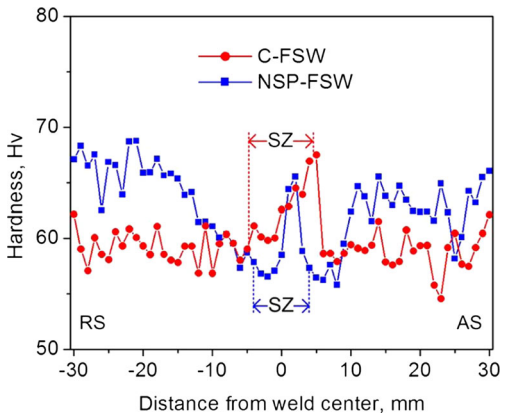

Fig. 9 Hardness profiles measured at the weld mid-thickness

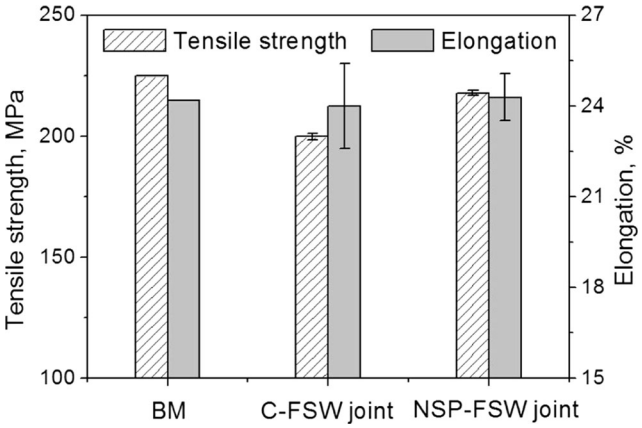

Fig. 10 Tensile properties of the joints

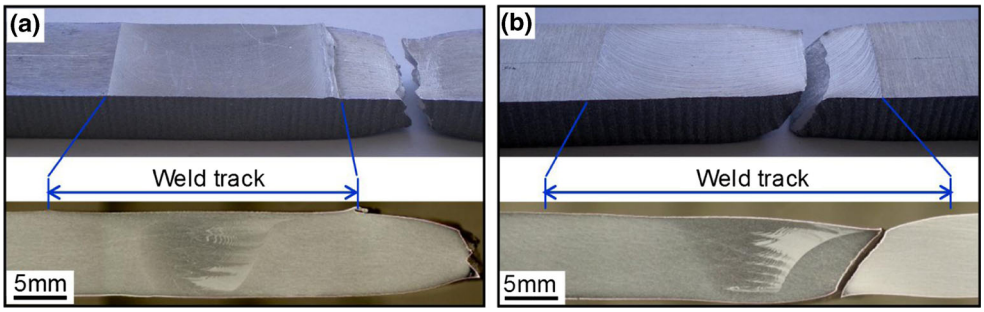

Fig. 11 Fracture locations of the joints: **a** C-FSW joint and **b** NSP-FSW joint

occurs in the weld track (see Fig. 11b), and the exact fracture location is also lying in the HAZ, which is identified by the grain structure features adjacent to the fracture path. Obviously, the fracture location of NSP-FSW joint is much nearer to the weld center than that of C-FSW joint, further confirming that the negative effect of welding thermal cycles has been reduced effectively by the NSP-FSW process.

The tensile behavior of FSW joints is largely related to the hardness profiles determined by microstructural evolutions, and the strength improvement by NSP-FSW can be explained as follows. On one hand, the fracture location of NSP-FSW joint presents relatively high hardness values in contrast to that of C-FSW joint, as seen from Figs. 9 and 11, which promotes the strain hardening capacity of the joint during tensile test and hence benefits to the strength improvement. On the other hand, the NSP-FSW joint has narrower softening region than the C-FSW joint. During tensile test, it is well known that the plastic deformation is primarily concentrated in the softening region [25, 26], and the borders of softening region would exert a constrained stress to the softening region material. For NSP-FSW joint with narrower softening region, smaller amount of grains are involved in the plastic deformation during tensile test, which accelerates the occurrence of work hardening under the effect of constrained stress and thus enhances the resistance to the subsequent deformation. That is to say, besides the increase of hardness minimum, the narrowing of softening region also contributes to the strength improvement of NSP-FSW joint.

4 Conclusions

Based on the present investigation, the conclusions of significance are drawn as follows:

1. Defect-free FSW joint is successfully produced under the condition of zero shoulder plunge depth by using a NSP welding tool. For NSP-FSW joint, the shoulder-affected zone almost completely disappears and the TMAZ shows a decrease in width when compared with the C-FSW joint.
2. Temperature measurement results indicate that in contrast to C-FSW, the welding thermal cycles around tool shoulder have been effectively controlled by the NSP-FSW process. Because of this, finer grains are obtained in the SZ and TMAZ; in addition, the grain coarsening, dislocation polygonization, and particle dissolution are all retarded in the HAZ.
3. Local softening occurs in the C-FSW joint and NSP-FSW joint. The softening region width of NSP-FSW joint is only nearly half that of C-FSW joint. The hardness profiles of the both joints show a W type with the lowest hardness region located in the HAZ. Comparatively, the hardness minimum of NSP-FSW joint is higher than that of C-FSW joint.
4. The strength efficiency of C-FSW joint is 89 %, while that of NSP-FSW joint reaches 97 %, indicating that the joint properties can be effectively improved by NSP-FSW. The fracture location of NSP-FSW joint is largely moved toward the weld center relative to that of C-FSW joint.

Acknowledgments The authors are grateful to be supported by the National Natural Science Foundation of China (Grant No. 51505471) and the Self-Determined Project for Youth of State Key Laboratory of Robotics, Shenyang Institute of Automation Chinese Academy of Sciences (Grant No. Y3A1209).

References

1. Nandan R, Debroy T, Bhadeshia HKDH (2008) Recent advances in friction-stir welding—process, weldment structure and properties. Prog Mater Sci 53:980–1023
2. Cam G, Mistikoglu S (2014) Recent developments in friction stir welding of Al-alloys. J Mater Eng Perform 23:1936–1953
3. Schmidt H, Hattel J, Wert J (2004) An analytical model for the heat generation in friction stir welding. Model Simul Mater Sci Eng 12: 143–157
4. Nandan R, Roy GG, Lienert TJ, Debroy T (2007) Three-dimensional heat and material flow during friction stir welding of mild steel. Acta Mater 55:883–895
5. Hilgert J, Schmidt HNB, dos Santos JF, Huber N (2011) Thermal models for bobbin tool friction stir welding. J Mater Process Technol 211:197–204
6. Fratini L, Buffa G, Shivpuri R (2010) Mechanical and metallurgical effects of in process cooling during friction stir welding of AA7075-T6 butt joints. Acta Mater 58:2056–2067

7. Liu HJ, Zhang HJ, Huang YX, Yu L (2010) Mechanical properties of underwater friction stir welded 2219 aluminum alloy. Trans Nonferrous Metals Soc China 20:1387–1391
8. Fu RD, Sun ZQ, Sun RC, Li Y, Liu HJ, Liu L (2011) Improvement of weld temperature distribution and mechanical properties of 7050 aluminum alloy butt joints by submerged friction stir welding. Mater Des 32:4825–4831
9. Papahn H, Bahemmat P, Haghpanahi M, Sommitsch C (2015) Study on governing parameters of thermal history during underwater friction stir welding. Int J Adv Manuf Technol 78:1101–1111
10. Ghetiya ND, Patel KM, Patel Anup B (2015) Prediction of temperature at weldline in air and immersed friction stir welding and its experimental validation. Int J Adv Manuf Technol 79:1239–1246
11. Elangovan K, Balasubramanian V, Babu S (2008) Developing an empirical relationship to predict tensile strength of friction stir welded AA2219 aluminum alloy. J Mater Eng Perform 17:820–830
12. Elangovan K, Balasubramanian V, Babu S (2009) Predicting tensile strength of friction stir welded AA6061 aluminium alloy joints by a mathematical model. Mater Des 30:188–193
13. Silva ACF, Braga DFO, de Figueiredo MAV, Moreira PMGP (2015) Ultimate tensile strength optimization of different FSW aluminium alloy joints. Int J Adv Manuf Technol 79:805–814
14. Ramulu PJ, Narayanan RG (2014) Influence of shoulder diameter, plunge depth, welding speed, rotational speed on the tensile behavior of friction stir welded AA 6061-T6 sheets. J Test Eval 42:1–13
15. Doude HR, Schneider JA, Nunes AC Jr (2014) Influence of the tool shoulder contact conditions on the material flow during friction stir welding. Metall MaterTrans A 45:4411–4422
16. Ramulu PJ, Narayanan RG, Kailas SV (2013) Forming limit investigation of friction stir welded sheets: influence of shoulder diameter and plunge depth. Int J Adv Manuf Technol 69:2757–2772
17. Zhang YN, Cao X, Larose S, Wanjara P (2012) Review of tools for friction stir welding and processing. Can Metall Q 51:250–261
18. Galvão I, Leal RM, Rodrigues DM, Loureiro A (2013) Influence of tool shoulder geometry on properties of friction stir welds in thin copper sheets. J Mater Process Technol 213:129–135
19. Jr LT, Heredia G, Rybicki D, Johannes LB (2015) Effect of tool shoulder features on defects and tensile properties of friction stir welded aluminum 6061-T6. J Mater Process Technol 219:271–277
20. Su JQ, Nelson TW, Mishra R, Mahoney M (2003) Microstructural investigation of friction stir welded 7050-T651 aluminum. Acta Mater 51:713–729
21. Prangnell PB, Heason CP (2005) Grain structure formation during friction stir welding observed by the "stop action technique". Acta Mater 53:3179–3192
22. Attallah MM, Davis CL, Strangwood M (2007) Microstructure-microhardness relationships in friction stir welded AA5251. J Mater Sci 42:7299–7306
23. Amini S, Amiri MR, Barani A (2015) Investigation of the effect of tool geometry on friction stir welding of 5083-O aluminum alloy. Int J Adv Manuf Technol 76:255–261
24. Threadgill PL, Leonard AJ, Shercliff HR, Withers PJ (2009) Friction stir welding of aluminium alloys. Int Mater Rev 54:49–93
25. Liu HJ, Fujii H, Maeda M, Nogi K (2003) Tensile properties and fracture locations of friction-stir-welded joints of 2017-T351 aluminum alloy. J Mater Process Technol 142:692–696
26. Zhang HJ, Liu HJ, Yu L (2011) Microstructural evolution and its effect on mechanical performance of joint in underwater friction stir welded 2219-T6 aluminium alloy. Sci Technol Weld Join 16:459–464